



# Magnetohydrodynamic Seismology of Quiet Solar Active Regions

Sergey A. Anfinogentov<sup>1</sup>  and V. M. Nakariakov<sup>2,3</sup> <sup>1</sup> Institute of Solar-Terrestrial Physics SB RAS, Lermontov St. 126, Irkutsk 664033, Russia<sup>2</sup> Centre for Fusion, Space and Astrophysics, Physics Department, University of Warwick, Coventry CV4 7AL, UK<sup>3</sup> St Petersburg Branch, Special Astrophysical Observatory, Russian Academy of Sciences, St. Petersburg, 196140, Russia

Received 2019 August 20; revised 2019 September 6; accepted 2019 September 25; published 2019 October 15

## Abstract

The ubiquity of recently discovered low-amplitude decayless kink oscillations of plasma loops allows for the seismological probing of the corona on a regular basis. In particular, in contrast to traditionally applied seismology that is based on the large-amplitude decaying kink oscillations excited by flares and eruptions, decayless oscillations can potentially provide the diagnostics necessary for their forecasting. We analyzed decayless kink oscillations in several distinct loops belonging to active region NOAA 12107 on 2010 July 10 during its quiet time period, when it was observed on the west limb in extreme ultraviolet by the Atmospheric Imaging Assembly on board the *Solar Dynamics Observatory*. The oscillation periods were estimated with the use of the motion magnification technique. The lengths of the oscillating loops were determined within the assumption of its semicircular shape by measuring the position of their footpoints. The density contrast in the loops was estimated from the observed intensity contrast accounting for the unknown spatial scale of the background plasma. The combination of those measurements allows us to determine the distribution of kink and Alfvén speeds in the active region. Thus, we demonstrate the possibility of obtaining seismological information about coronal active regions during the quiet periods of time.

*Unified Astronomy Thesaurus concepts:* [Solar coronal seismology \(1994\)](#); [Solar magnetic fields \(1503\)](#); [Solar coronal waves \(1995\)](#); [Solar active region magnetic fields \(1975\)](#); [Solar coronal loops \(1485\)](#); [Solar oscillations \(1515\)](#)

## 1. Introduction

Active regions of the solar corona are regions of the enhanced plasma density penetrated by a closed magnetic field. In the extreme-ultraviolet (EUV) band, active regions are seen as localized bundles of bright plasma loops that are believed to highlight certain magnetic flux tubes. Active regions are known to host sporadic impulsive energy releases observed as solar flares and coronal mass ejections that are the most powerful physical phenomena in the solar system. Robust forecasting of flares and mass ejections is an important element of space weather research. The key required parameter is the magnetic field. But the direct observational measurement of the coronal magnetic field is possible in some specific cases only because of the intrinsic difficulties connected with the high temperature and low concentration of the coronal plasma. One promising indirect method for obtaining information about the coronal magnetic field is magnetohydrodynamic (MHD) seismology, based on the estimation of the coronal Alfvén speed (e.g., Nakariakov & Ofman 2001; Liu & Ofman 2014; Wang 2016). Similar plasma diagnostic techniques are used in laboratory plasma and Earth's magnetospheric research (e.g., Fasoli et al. 2002; Nakariakov et al. 2016b, respectively).

A suitable seismological probe of the Alfvén speed in an active region is a kink (transverse) oscillation of a coronal loop (e.g., Roberts et al. 1984). Kink oscillations are excited by low coronal eruptions, and decay in several oscillation cycles (e.g., Zimovets & Nakariakov 2015). The spatially resolving detection of the kink oscillation allowed for the interpretation of the oscillation as the fundamental harmonic of a standing  $m = 1$  fast magnetoacoustic mode of the coronal loop. The plausibility of this estimation is confirmed by the observationally established linear scaling of the kink oscillation period with the loop length (Goddard et al. 2016) and the variety of

the oscillation periods detected in different loops belonging to the same bundle (Li et al. 2017). The first seismological estimation of the magnetic field in a coronal loop by a kink oscillation was performed by Nakariakov & Ofman (2001). The ratio of the wavelength that for the fundamental harmonic is double the length of the loop, and the observationally determined oscillation period gives the phase speed. As the wavelength is much longer than the minor radius of the oscillating loop, it is possible to use the theoretical estimation of the phase speed as the kink speed (Ryutov & Ryutova 1976; Edwin & Roberts 1983). Together with the independent estimation of the density contrast in the loop, this quantity gives the estimation of the local Alfvén speed. If there is an independent estimation of the plasma density in the loop, one gets the estimation of the absolute value of the field. An important advantage of MHD seismology by kink oscillations is a clear association of the observed oscillation with a specific plasma structure, which makes the diagnostics free of the line-of-sight integration shortcomings. Moreover, seismology allows for estimating the Alfvén speed and field in off-limb active regions where the field could not be determined by extrapolation.

In addition, the detection of multimodal kink oscillations has led to the development of kink-based seismological techniques for the estimation of the relative density stratification, based on the ratios of the periods of different harmonics (e.g., Andries et al. 2005; Van Doorselaere et al. 2007). The transverse profile of the density in the loop could be estimated with the use of another observable parameter, the damping time (e.g., Van Doorselaere et al. 2004). Serious progress in coronal seismology by kink oscillations has recently been achieved with the application of the Bayesian statistics (Arregui et al. 2015; Goddard et al. 2018); see also Arregui (2018) for a recent

review. An important tool for testing the theoretical results against observations is forward modeling of observables (Yuan & Van Doorsselaere 2016a, 2016b). The observed combination of two damping regimes, the exponential and Gaussian regimes (Pascoe et al. 2012), allowed for the development of seismological techniques for the estimation of the transverse profile of the plasma density in the oscillating loop (Pascoe et al. 2018, 2016, 2019), and its evolution in the course of the oscillation (Goddard et al. 2018). Certain theoretical shortcomings of the latter techniques have recently been discussed in (Arregui & Goossens 2019). However, the main disadvantage of the seismology by decaying kink oscillations is their occurrence after an impulsive energy release, usually the low coronal eruption (Zimovets & Nakariakov 2015), which excites the oscillations. This intrinsic difficulty does not allow for the diagnostics of the plasma before the eruption, which would be of interest in the context of space weather forecasting.

Another, decayless regime of kink oscillations was discovered by Wang et al. (2012). Oscillations of this kind are a ubiquitous and persistent feature of “quiet” active regions (Anfinogentov et al. 2013, 2015), i.e., they appear in the nonactive periods of time. Typical oscillation periods are from a few to several minutes. The periods are found to scale linearly with the length of the oscillating loop, justifying their interpretation as standing kink modes of coronal loops. Moreover, Nisticò et al. (2013) demonstrated that the same loop oscillates in different periods of time in both decay and decayless regimes with the same oscillation period. Oscillations of this type are possibly detected in flaring loops as well (Li et al. 2018), and could explain persistent oscillatory variations of the Doppler shift detected in EUV spectral observations by Tian et al. (2012). The mechanisms responsible for the sustainability of the oscillations, i.e., counteracting the damping by, e.g., resonant absorption, and hence determining the oscillation amplitude are still debated (e.g., Hindman & Jain 2014; Murawski et al. 2015; Antolin et al. 2016; Nakariakov et al. 2016a; Guo et al. 2019; Karamelas et al. 2019). An intrinsic difficulty in the observational study of decayless kink oscillations is that their typical projected displacement amplitudes are lower than 1 Mm, and often smaller than the pixel size of available EUV imagers. Nevertheless, these oscillations are robustly detected with the use of the recently designed motion magnification technique (Anfinogentov & Nakariakov 2016). In particular, with the use of this technique, the coexistence of the fundamental and second spatial harmonics of decayless kink oscillations has been revealed in Duckenfield et al. (2018). The persistent occurrence of decayless kink oscillations in coronal active regions before flares and eruptions makes them a promising seismological tool that can provide us with important input parameters for space weather forecasting techniques.

In this Letter, we present the first seismological diagnostics of the Alfvén speed in an active region during a nonflaring period of time, i.e., in a quiet active region.

## 2. Observations

For our study, we selected active region NOAA 12107 observed on the west limb of the Sun on 2010 July 10. The active region was seen as a set of coronal loops of different heights, lengths, and orientations. Several loops are seen to be well contrasted in the 171 Å channel. We use a 3 hr series of *Solar Dynamics Observatory* (SDO)/AIA images recorded from 14:00 UT until 17:00 UT. No flares or eruptions were observed in the active region or its vicinity during this time

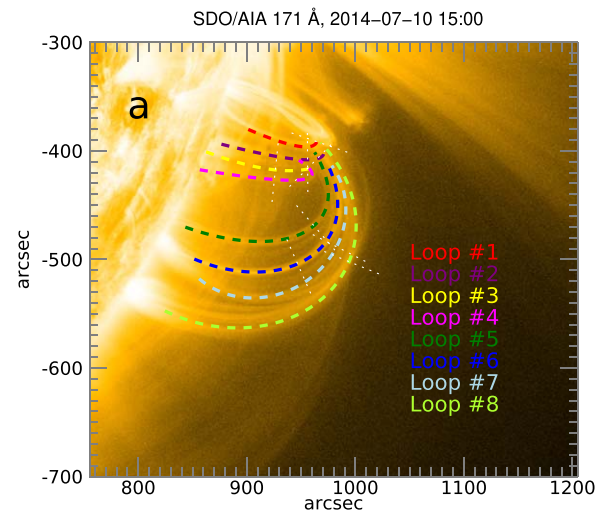


**Figure 1.** EUV image of AR 12107 observed by SDO/AIA at 171 Å on 2014 July 10 at 14:32 UT (background). Coronal loops selected for the analysis are overplotted with the colored dashed lines. Artificial slits used for creating time–distance plots are marked with the straight dotted lines.

interval. The images were downloaded from the SDO data processing center<sup>4</sup> with the use of the provided online service for cutting out the region of interest. As the analyzed active region was located on the solar limb, there was no need for its tracking or derotation. For a detailed analysis, we selected eight coronal loops indicated in Figure 1 with dashed lines of different colors. In Figure 1, we show an EUV image of the active region NOAA 12107 taken on 2014 July 10 at 14:32 UT.

## 3. Data Analysis

### 3.1. Detecting Oscillations Using Motion Magnification

Decayless kink oscillations are observed to have the displacement amplitude of the order of 0.2 Mm (Anfinogentov et al. 2015), which is less than the pixel size of SDO/AIA. The analysis of the oscillations was performed by processing the imaging data cubes using the motion magnification technique (Anfinogentov & Nakariakov 2016) based on the Dual Complex Wavelet Transform (DCWT). Each image is decomposed into a set of complex wavelet components corresponding to different spatial scales, positions, and orientations. The phase of the complex wavelet coefficients reflects the spatial location of different structures in the image and is sensitive to very small displacements of these structures in the next image. So, the algorithm tracks variations of the phase and amplifies it in a certain broad range of periods. Performing the inverse DCWT, we obtain a new series of images where all spatial displacements are magnified by a prescribed factor that is called the magnification coefficient.

In this work, we use the magnification coefficient of 5. We found this value optimal for our data set, since it makes the transverse oscillations well visible in time–distance maps in the well-contrasted loops on one hand, and does not introduce significant distortion to the images on the other hand.

### 3.2. Time–Distance Maps

To make a time–distance map for an oscillating loop, we choose the instance of time where the loop has the best contrast

<sup>4</sup> <http://jsoc.stanford.edu/>

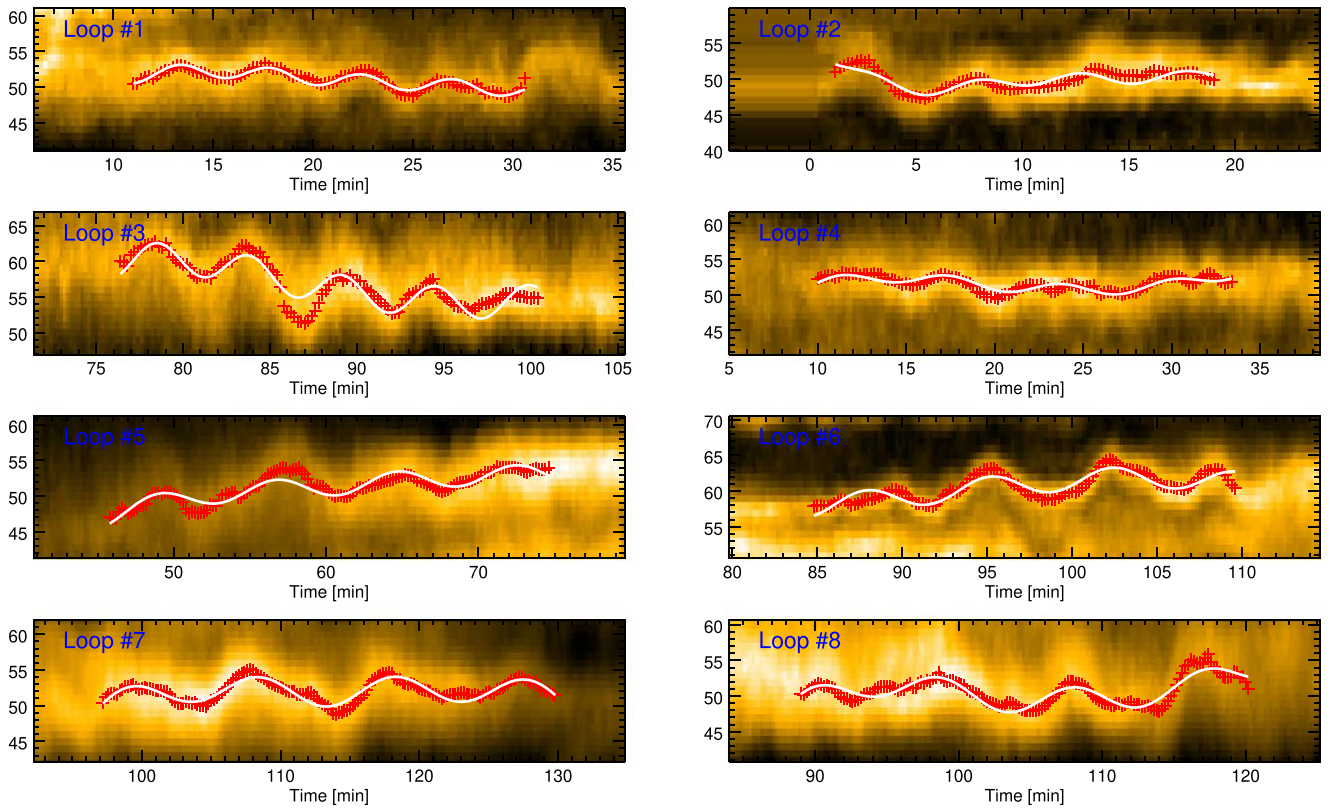


**Figure 2.** Time–distance plots showing decayless kink oscillations observed in eight loops selected in AR 12107. The kink (transverse) motions in the image sequence were magnified by a factor of 5. The instant of time when the loops appear to be best contrasted in 171 Å images are marked with vertical green lines. Images taken at these times were used as a reference to estimate the length of the loops.

**Table 1**  
Estimation of the Alfvén Speed by Decayless Kink Oscillations

Loop No	Loop Length (Mm)	Slit Width (px)	Period (s)	Intensity Contrast	Density Contrast	Kink Speed (km s <sup>-1</sup> )	$C_{A0}$ (km s <sup>-1</sup> )	$C_{Ae}$ (km s <sup>-1</sup> )
1	224	1	276 <sup>+2.8</sup> <sub>-2.5</sub>	0.23	0.04 <sup>+0.35</sup> <sub>-0.03</sub>	1622 <sup>+15</sup> <sub>-17</sub>	1173 <sup>+182</sup> <sub>-23</sub>	4313 <sup>+7935</sup> <sub>-2156</sub>
2	231	5	334 <sup>+40</sup> <sub>-49</sub>	0.46	0.07 <sup>+0.40</sup> <sub>-0.05</sub>	1395 <sup>+226</sup> <sub>-163</sub>	942 <sup>+338</sup> <sub>-35</sub>	2765 <sup>+4221</sup> <sub>-1076</sub>
3	244	11	321 <sup>+11</sup> <sub>-7.8</sub>	0.66	0.11 <sup>+0.52</sup> <sub>-0.04</sub>	1525 <sup>+38</sup> <sub>-52</sub>	1140 <sup>+240</sup> <sub>-38</sub>	2122 <sup>+2156</sup> <sub>-384</sub>
4	235	5	382 <sup>+18</sup> <sub>-15</sub>	0.70	0.12 <sup>+0.57</sup> <sub>-0.04</sub>	1228 <sup>+49</sup> <sub>-58</sub>	927 <sup>+218</sup> <sub>-43</sub>	1549 <sup>+1514</sup> <sub>-184</sub>
5	292	28	475 <sup>+10</sup> <sub>-10</sub>	0.50	0.08 <sup>+0.42</sup> <sub>-0.06</sub>	1229 <sup>+25</sup> <sub>-25</sub>	903 <sup>+161</sup> <sub>-27</sub>	1974 <sup>+3578</sup> <sub>-466</sub>
6	329	5	435 <sup>+12</sup> <sub>-11</sub>	0.43	0.07 <sup>+0.43</sup> <sub>-0.05</sub>	1512 <sup>+39</sup> <sub>-42</sub>	1110 <sup>+201</sup> <sub>-38</sub>	2624 <sup>+5352</sup> <sub>-769</sub>
7	343	15	580 <sup>+6.7</sup> <sub>-6.6</sub>	0.42	0.06 <sup>+0.43</sup> <sub>-0.04</sub>	1184 <sup>+14</sup> <sub>-14</sub>	866 <sup>+155</sup> <sub>-21</sub>	1948 <sup>+4051</sup> <sub>-489</sub>
8	391	13	547 <sup>+9.0</sup> <sub>-8.5</sub>	0.26	0.04 <sup>+0.37</sup> <sub>-0.03</sub>	1429 <sup>+22</sup> <sub>-23</sub>	1030 <sup>+174</sup> <sub>-19</sub>	3353 <sup>+6682</sup> <sub>-1478</sub>

in the 171 Å channel, and put an artificial slit across the loop near its apex. The slit position and width were manually selected individually for each loop to make the observed oscillation more evident. The slit positions are indicated in Figure 1, and their widths are listed in Table 1. In Figure 2, we show time–distance maps obtained with the use of this technique for the selected loops. The motion magnification allowed us to make the oscillatory patterns clearly visible in time–distance maps for all eight loops.

### 3.3. Estimation of the Density Contrast Using Bayesian Inference

To estimate the density contrast inside and outside the oscillating loop, we assume that the loop and its neighborhood are isothermal, and the observed emission is optically thin.

Thus, we model the density profile by a step function

$$n(r) = \begin{cases} n_0, & r < l_0 \\ n_e, & l_0 < r < l_e \\ 0, & r > l_e \end{cases} \quad (1)$$

where  $n_0$  and  $n_e$  are number densities inside and outside the loop, respectively;  $l_0$  is the column depth of the loop segment, connected with the minor radius of the loop, and  $l_e$  is the column depth of the background plasma along the line of sight. The value of  $l_e$  is expected to be much longer than the minor radius of the loop, i.e., comparable to the active region size. Note that the estimation of the kink speed requires the value of the external number density  $n_e$  in the vicinity of the loop. The parameter  $l_e$  is introduced to account for the emitting plasma

located along the line of sight ahead and behind the oscillating loop.

Within this model the EUV intensity of the loop,  $I_0$ , and the background,  $I_e$ , are calculated as

$$I_e = G(\lambda, T)l_e(\eta n_0)^2, \quad (2)$$

$$I_0 = G(\lambda, T)[(l_e - l_0)(\eta n_0)^2 + l_0 n_0^2], \quad (3)$$

where  $\eta = n_e/n_0$  is the density contrast and  $G(\lambda, T)$  is the contribution function that depends upon the observed wavelength and the temperature of the emitting plasma, and accounts for specific properties of the instrument (e.g., *SDO/AIA*). In our case, we model only the dependence of the intensity contrast upon the density contrast and, therefore, are not interested in the absolute values. Thus, for an isothermal plasma, we can safely take  $G(\lambda, T) = 1$  and  $l_0 = 1$ .

To estimate the density contrast from the observed intensities  $\mathcal{I}_0$  and  $\mathcal{I}_e$ , which are the modeled intensities  $I_0$  and  $I_e$  contaminated by the noise, we use the Bayesian analysis in combination with Markov Chain Monte Carlo (MCMC) sampling. In our model, we assume that the measurement errors are normally distributed and independent in different pixels, obtaining the likelihood function

$$P(\mathcal{I}_0, \mathcal{I}_e|\theta) = \frac{\exp\left[-\frac{(\mathcal{I}_e - I_e(\theta))^2}{\sigma_e}\right] \exp\left[-\frac{(\mathcal{I}_0 - I_0(\theta))^2}{\sigma_0}\right]}{2\pi\sigma_e\sigma_0}, \quad (4)$$

where  $\theta = [n_0, \eta, l_e]$  is the set of free model parameters,  $\sigma_0$  and  $\sigma_e$  are the measurement errors, and  $I_e(\theta)$  and  $I_0(\theta)$  are the modeled intensities given by Equations (2) and (3). In this work, we use uniform priors with the following ranges: [0, 1] for the density contrast  $\eta$ ; [10, 200] for the background length scale  $l_e$ ; and [0, 2] for the normalized internal density  $n_0$ .

The intensity values  $I_e$  and  $I_0$  are obtained from the original *SDO/AIA* images (before the motion magnification) taken at the times when the oscillatory patterns shown in Figure 2 were detected. The measurement uncertainties  $\sigma_0$ , and  $\sigma_e$  are estimated using the `AIA_BP_ESTIMATE_ERROR` function from the SolarSoft package (Freeland & Handy 1998). Both the intensities and the corresponding errors were then normalized to such as  $I_0 = 1$ .

To sample the posterior probability distribution, we use our Solar Bayesian Analysis Toolkit (SoBAT) code, which is available online at <https://github.com/Sergey-Anfinogentov/SoBAT>. The description of the code can be found in Pascoe et al. (2017). For each analyzed loop, we generated  $10^6$  samples and used them to find the most probable value of  $\eta$ . The credible intervals are defined as 5% and 95% percentiles and correspond to the confidence level of 90%.

### 3.4. Estimating the Alfvén Speed

First, we estimate the position of the oscillating loop at each instant of time by fitting a Gaussian to the transverse intensity profile of the loop extracted from the time–distance map. To estimate the period and the corresponding uncertainties from the obtained data points, we use the Bayesian analysis. Transverse displacements of each loop were modeled by a sinusoidal function on top of a polynomial trend. The measurement errors are assumed to be normally distributed and individually independent.

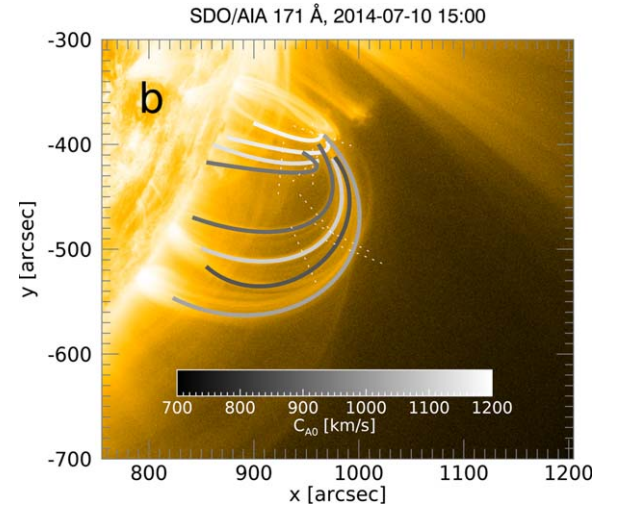


**Figure 3.** Mapping the Alfvén speed in AR 12107. The color of the broad curved lines following the coronal loops shows the internal Alfvén speed  $C_{A0}$  estimated from the observed decayless kink oscillations. The EUV image of AR 12107 observed by *SDO/AIA* at 171 Å on 2014 July 10 at 14:32 UT is used as the background. Artificial slits used for creating time–distance plots are marked with the straight dotted lines.

We generate  $10^6$  samples from the posterior distribution using the SoBAT MCMC code. For all free parameters we use uniform priors. The kink speed  $C_k$  is then estimated from the oscillation period

$$C_k = \frac{2L}{P}, \quad (5)$$

where  $L$  is the length of the oscillating loop estimated by the apparent position of the loop footpoints and its apex in the assumption of the semicircular shape of the loop. To account for the uncertainties coming from the period measurements we computed  $C_k$  for each of  $10^6$  samples from the posterior distribution of the oscillation period  $P$ . It allows us to estimate the most probable value and the credible intervals for the kink speed, and transparently trace the propagation of the estimated uncertainties in the estimation of the Alfvén speed.

The kink speed and density contrast allow us to estimate the external and internal Alfvén speeds as

$$C_{A0} = C_k / \sqrt{2/(1 + \eta)}, \quad (6)$$

$$C_{Ae} = C_{A0} / \sqrt{\eta}, \quad (7)$$

respectively (e.g., Nakariakov & Ofman 2001). The credibility of this technique was demonstrated by Verwichte et al. (2013) for decaying kink oscillations. To account for the uncertainties coming from the measurements of the density contrast  $\eta$  and the oscillation period, we calculate  $C_{Ae}$  and  $C_{A0}$  for each of  $10^6$  samples obtained with MCMC for the density contrast  $\eta$  and the oscillation period  $P$ . The most probable values of  $C_{Ae}$  and  $C_{A0}$  are defined as the maximums of the corresponding histograms, and the 90% credible intervals are calculated as the 5th and 95th percentiles.

### 3.5. Mapping the Alfvén Speed in the Corona

The detection of kink oscillations in different coronal loops with different heights and lengths allows us to make spatially resolved estimates of the Alfvén speed in the active region. The

estimation requires the knowledge of the loop lengths, oscillation periods corresponding to the fundamental kink mode, and the density contrasts in the oscillating loops (see Nakariakov & Ofman 2001 and Section 3.4). The oscillation period is estimated directly from the time–distance maps, while the observed intensity contrast inside and outside the oscillating loop gives us a proxy for the density contrast. The length of the oscillating loop is estimated from the position of its footpoints.

For the eight chosen coronal loops, we estimated the internal and external Alfvén speeds and the corresponding uncertainties. Our estimates are summarized in Table 1. Note that despite the huge uncertainty in the density contrast estimations we successfully obtained reliable measurements of the Alfvén speed inside oscillating loops with an accuracy of 15%–20%. In Figure 3, we show a spatially resolved mapping of the internal Alfvén speed inferred from the decayless kink oscillations. The given values should be understood as values averaged along the oscillating loops; therefore, the color corresponding to the Alfvén speed value is evenly distributed along each loop.

#### 4. Discussion

We demonstrated that decayless kink oscillations processed by the pioneering motion magnification technique allow one to map the Alfvén speed in the solar corona during the quiet time period. The analysis of the EUV emission from active region 12107 produced the first-ever seismogram of a solar coronal active region during its quiet period, showing the spatial distribution of the Alfvén speed. The seismogram is presented in Figure 3. Note that the quantities shown in Figure 3 correspond to the values averaged along the oscillating loops, as the effect of the plasma stratification in this study was neglected. However, further accounting for higher spatial harmonics of decayless kink oscillations (Duckenfield et al. 2018) would allow for mapping the Alfvén speed along the loops.

Relatively large errors in the estimations of the density contrast from the observed intensity contrast lead to a very uncertain estimate of the Alfvén speed in the plasma outside the loops (see Table 1). However, the Alfvén speed inside the oscillating loop can be measured with the precision of about 15%–20%. Even lower uncertainties can be achieved if more precise measurements of the density contrast are available in the same active region either spectroscopically or by seismology based on decaying kink oscillations (e.g., Pascoe et al. 2016, 2018). Note that the less uncertain Alfvén speed inside the oscillating loop is more informative, since it can be recalculated to the magnetic field strength after independently measuring the plasma density in the loop, while measuring the density of the background plasma is far more complicated. The density of a coronal loop can be obtained, for example, using the forward-modeling approach (Goddard et al. 2018) or from the analysis of the differential emission measure (see, e.g., Aschwanden et al. 2013). Even if the robust estimation of the plasma density is not possible, the estimation of the Alfvén speed is important for, for example, understanding the interaction of global coronal waves with the active region hosting the oscillating loops (e.g., Long et al. 2017). In addition, further improvement of the method can be achieved by making a more precise estimation of the length of the oscillating loop (see, e.g., Aschwanden 2011).

In addition, we demonstrated that decayless kink oscillations can be detected in many loops within a single active region with the use of presently available EUV images provided by *SDO/AIA*. This detection allows us to carry out spatially resolved measurements of the Alfvén speed and, hence, potentially, the coronal magnetic field during the quiet time periods.

We should emphasize that the coronal seismology based on decayless kink oscillations such as those presented here can be performed routinely for almost every active region observed on the Sun, since decayless kink oscillations are a ubiquitous phenomenon (Anfinogentov et al. 2015) and are detected almost always in most of the active regions.

The obtained results may be considered as the first step toward the routine estimation of the Alfvén speed and, potentially, of the magnetic field and free magnetic energy available for the release, in particular, in preflaring active regions.

This work was supported by the Russian Scientific Foundation grant No. 18-72-00144 (S.A.A.; Data Analysis sections, processing data and preparing figures, interpretation of the obtained results). V.M.N. (Introduction and Discussion sections, interpretation of the obtained results) acknowledges support from the STFC consolidated grant No. ST/P000320/1 and from the Russian Foundation for Basic Research grant No. 18-29-21016. The authors thank the *SDO/AIA* team.

*Facility:* *SDO/AIA*.

*Software:* IDL, SolarSoft, DTCWT based motion magnification (Anfinogentov & Nakariakov 2016; Anfinogentov et al. 2019), Python implementation of DTCWT (Wareham & Cotter 2017), Solar Bayesian Analysis Toolkit.

#### Competing Interests

The authors declare that they have no conflicts of interests.

#### ORCID iDs

Sergey A. Anfinogentov  <https://orcid.org/0000-0002-1107-7420>

V. M. Nakariakov  <https://orcid.org/0000-0001-6423-8286>

#### References

- Andries, J., Arregui, I., & Goossens, M. 2005, *ApJL*, 624, L57
- Anfinogentov, S., Nakariakov, V., & Kosak, K. 2019, DTCWT based motion magnification, v0.5.0, Zenodo, doi:10.5281/zenodo.3368774
- Anfinogentov, S., & Nakariakov, V. M. 2016, *SoPh*, 291, 3251
- Anfinogentov, S., Nisticò, G., & Nakariakov, V. M. 2013, *A&A*, 560, A107
- Anfinogentov, S. A., Nakariakov, V. M., & Nisticò, G. 2015, *A&A*, 583, A136
- Antolin, P., De Moortel, I., Van Doorselaere, T., & Yokoyama, T. 2016, *ApJL*, 830, L22
- Arregui, I. 2018, *AdSpR*, 61, 655
- Arregui, I., & Goossens, M. 2019, *A&A*, 622, A44
- Arregui, I., Soler, R., & Asensio Ramos, A. 2015, *ApJ*, 811, 104
- Aschwanden, M. J. 2011, *LRSP*, 8, 5
- Aschwanden, M. J., Boerner, P., Schrijver, C. J., & Malanushenko, A. 2013, *SoPh*, 283, 5
- Duckenfield, T., Anfinogentov, S. A., Pascoe, D. J., & Nakariakov, V. M. 2018, *ApJL*, 854, L5
- Edwin, P. M., & Roberts, B. 1983, *SoPh*, 88, 179
- Fasoli, A., Testa, D., Sharapov, S., et al. 2002, *PPCF*, 44, B159
- Freeland, S. L., & Handy, B. N. 1998, *SoPh*, 182, 497
- Goddard, C. R., Antolin, P., & Pascoe, D. J. 2018, *ApJ*, 863, 167
- Goddard, C. R., Nisticò, G., Nakariakov, V. M., & Zimovets, I. V. 2016, *A&A*, 585, A137
- Guo, M., Van Doorselaere, T., Karampelas, K., et al. 2019, *ApJ*, 870, 55
- Hindman, B. W., & Jain, R. 2014, *ApJ*, 784, 103

- Karamelas, K., Van Doorselaere, T., Pascoe, D. J., Guo, M., & Antolin, P. 2019, *FrASS*, **6**, 38
- Li, D., Yuan, D., Su, Y. N., et al. 2018, *A&A*, **617**, A86
- Li, H., Liu, Y., & Vai Tam, K. 2017, *ApJ*, **842**, 99
- Liu, W., & Ofman, L. 2014, *SoPh*, **289**, 3233
- Long, D. M., Bloomfield, D. S., Chen, P. F., et al. 2017, *SoPh*, **292**, 7
- Murawski, K., Solov'ev, A., Kraškievich, J., & Srivastava, A. K. 2015, *A&A*, **576**, A22
- Nakariakov, V. M., Anfinogentov, S. A., Nisticò, G., & Lee, D.-H. 2016a, *A&A*, **591**, L5
- Nakariakov, V. M., & Ofman, L. 2001, *A&A*, **372**, L53
- Nakariakov, V. M., Pilipenko, V., Heilig, B., et al. 2016b, *SSRv*, **200**, 75
- Nisticò, G., Nakariakov, V. M., & Verwichte, E. 2013, *A&A*, **552**, A57
- Pascoe, D. J., Anfinogentov, S., Nisticò, G., Goddard, C. R., & Nakariakov, V. M. 2017, *A&A*, **600**, A78
- Pascoe, D. J., Anfinogentov, S. A., Goddard, C. R., & Nakariakov, V. M. 2018, *ApJ*, **860**, 31
- Pascoe, D. J., Goddard, C. R., Nisticò, G., Anfinogentov, S., & Nakariakov, V. M. 2016, *A&A*, **589**, A136
- Pascoe, D. J., Hood, A. W., de Moortel, I., & Wright, A. N. 2012, *A&A*, **539**, A37
- Pascoe, D. J., Hood, A. W., & Van Doorselaere, T. 2019, *FrASS*, **6**, 22
- Roberts, B., Edwin, P. M., & Benz, A. O. 1984, *ApJ*, **279**, 857
- Ryutov, D. A., & Ryutova, M. P. 1976, *JETP*, **43**, 491
- Tian, H., McIntosh, S. W., Wang, T., et al. 2012, *ApJ*, **759**, 144
- Van Doorselaere, T., Andries, J., Poedts, S., & Goossens, M. 2004, *ApJ*, **606**, 1223
- Van Doorselaere, T., Nakariakov, V. M., & Verwichte, E. 2007, *A&A*, **473**, 959
- Verwichte, E., Van Doorselaere, T., Foullon, C., & White, R. S. 2013, *ApJ*, **767**, 16
- Wang, T., Ofman, L., Davila, J. M., & Su, Y. 2012, *ApJL*, **751**, L27
- Wang, T. J. 2016, *GMS*, **216**, 395
- Wareham, R., Cotter, F., scf32, et al. 2017, rjw57/dtcwt: v0.12.0, Zenodo, doi:10.5281/zenodo.889246
- Yuan, D., & Van Doorselaere, T. 2016a, *ApJS*, **223**, 23
- Yuan, D., & Van Doorselaere, T. 2016b, *ApJS*, **223**, 24
- Zimovets, I. V., & Nakariakov, V. M. 2015, *A&A*, **577**, A4